RESEARCH ARTICLE | MARCH 01 2023

Experimental investigation on cylinder noise and its reductions by identifying aerodynamic sound sources in flow fields

Chuntai Zheng (郑春泰); Peng Zhou (周朋); Siyang Zhong (钟思阳); Xin Zhang (张欣)

Physics of Fluids 35, 035103 (2023)
https://doi.org/10.1063/5.0138080

Experimental investigation on cylinder noise and its reductions by identifying aerodynamic sound sources in flow fields

Cite as: Phys. Fluids **35**, 035103 (2023); doi: 10.1063/5.0138080
Submitted: 8 December 2022 · Accepted: 10 February 2023 ·
Published Online: 1 March 2023

Chuntai Zheng (郑春泰),[1] Peng Zhou (周朋),[1] Siyang Zhong (钟思阳),[2] and Xin Zhang (张欣)[1,a)]

AFFILIATIONS

[1] Department of Mechanical and Aerospace Engineering, The Hong Kong University of Science and Technology, Clear Water Bay, Kowloon, Hong Kong, China
[2] Department of Aeronautical and Aviation Engineering, The Hong Kong Polytechnic University, Hung Hom, Kowloon, Hong Kong, China

[a)] Author to whom correspondence should be addressed: aexzhang@ust.hk

ABSTRACT

Through anechoic wind tunnel tests, this study comprehensively investigates the noise and drag reductions on a circular cylinder with dimples. Dimples built on a surface pattern fabric cover the cylinder surface as one of the passive flow control methods. The force, noise, and flow field measurements are performed at diameter-based Reynolds numbers ranging from 3×10^4 to 1.3×10^5, covering the sub-critical, critical, and supercritical regimes. The force and noise measurement results show that dimple fabric simultaneously reduces noise and drag in the critical regime. The changes in flow structures were characterized by the Time-resolved Particle Image Velocimetry (TR-PIV) measurements. Based on the vortex sound theory, the flow analysis shows that the dominant sound sources are found to be concentrated near the cylinder surface, which is caused by the unsteady vortex motions near the separation locations during the process of vortex shedding. The cross-correlation between the synchronized TR-PIV and microphone measurements further supports the conclusions. Moreover, the cylinder noise reductions controlled by the dimples are directly associated with the reduced sound sources in the critical and supercritical regimes, corresponding to the reduced strength of the vortex shedding.

I. INTRODUCTION

Over the last decades, a large number of studies have been carried out to control drag forces and noises on a circular cylinder.[1] The drag reductions on a circular cylinder can be achieved by means of surface modifications, such as adding sand-grid surface roughness,[2] grooves,[3–6] dimples,[7] and helical wire.[8] The drag reductions of these methods mainly rely on delaying flow separations by forcing a boundary-layer transition to turbulence. There are also noise reduction methods for cylinder flow by using porous materials,[9,10] a splitter plate,[11,12] wavy structures,[13] helical cables,[14] and grooves.[3,6] The noise reductions from those methods mainly rely on suppression of Aeolian tone caused by the vortex shedding.[15]

Understanding the flow mechanism of cylinder noise and drag reductions is very important, as the flow over a circular cylinder represents the aerodynamic and aeroacoustic characteristics of a flow over a bluff body, by which the cylinder flow control methods can be extended to the practical engineering applications, e.g., control of flow over a pantograph of a train.[16] Based on the flow field measurements, previous studies widely explain noise reductions by the decreased velocity fluctuations caused by the vortex shedding in the near wake.[3,10,17] However, since the intensive velocity fluctuations are formed away from the cylinder surface, they cannot be used to establish direct connections between the far-field sound pressure and the near flow fields. Alternatively, the vortex sound theory, originated by Powell[18] and extended by Howe,[19] can be used to theoretically establish the direct connections between the cylinder noise and the generation and convection of vorticity, which is referred to as sound sources in the flow field. However, experimentally identifying sound sources in the flow fields requires flow measurements to provide sufficient spatial and time resolutions, which is still challenging. For this reason, the experimental investigations on the sound sources in flow fields are still rare.[20,21] To the authors' knowledge, no experimental research has been done to explain cylinder noise reductions by comprehensively investigating the sound sources in flow fields.

In this study, dimples built on a piece of fabric are used to control drag and noise on a circular cylinder. The effects of drag and noise control are investigated by the force balance and microphone measurements in an anechoic wind tunnel. Based on the noise and drag characteristics, the flow regimes are classified in different Reynolds number ranges. Time-resolved Particle Image Velocimetry (TR-PIV) is used to measure the flow fields, providing sufficient spatial and time resolutions. We further apply the vortex sound theory to the flow analysis, aiming to establish the direct connections between the cylinder noise reductions and sound sources in flow fields. This study helps to further enhance the understanding of noise and drag reductions on a circular cylinder, which potentially leads to better applications of noise and drag reduction methods.

In the remainder of this paper, Sec. II presents a theoretical model of the vortex sound theory; Sec. III introduces the setup of wind tunnel tests; Sec. IV shows the drag and the noise control effects of a circular cylinder with dimples; Sec. V shows the TR-PIV measurement results, based on which discussions are made on the mechanism for the cylinder noise and noise reductions; and Sec. VI provides the conclusions.

II. VORTEX SOUND THEORY

According to the vortex sound theory,[18,22] force applied to the fluid by a cylinder surface can be defined in terms of the volume distributions of the Lamb vector $\boldsymbol{\omega} \times \boldsymbol{v}$, where $\boldsymbol{\omega}$ is the vorticity vector and $\boldsymbol{v}$ is the velocity vector. Then, the solution of acoustic pressure $p(\boldsymbol{r}, t)$ can be written as[18,22]

$$p(\boldsymbol{r}, t) \approx \frac{-\rho r_i}{4\pi c_\infty |\boldsymbol{r}|^2} \int_V \frac{\partial}{\partial t}(\boldsymbol{\omega} \times \boldsymbol{v})(\boldsymbol{x}, \tau) \cdot \nabla Y_i(\boldsymbol{x}) \mathrm{d}V, \qquad (1)$$

where c_∞ is the sound speed, $\boldsymbol{r}$ is the distance vector between the microphone and sound sources, ρ is the air density, τ is the retarded time defined as $\tau = t - |\boldsymbol{r}|/c_\infty$, $\boldsymbol{x}$ is the flow field coordinate vector (x, y, z), Y_i is the i th component of Kirchhoff vector, and V is the wake region.

In practical application, where the region within the view of the TR-PIV is finite, Y_i can be replaced with the velocity potential φ_i,[23] which is produced by a rigid body's transitional motion at a unit speed. The amplitude of the φ_i around a cylinder represents the acoustic radiation efficiency.[23]

For a cylinder flow, the dipole noise source is dominant along the line between two monopole sources, which defines the dipole axis (y-axis), and the far-field sound pressure at the microphone location of 90° is mainly caused by the lift force fluctuations along y-axis. Moreover, the $\boldsymbol{\omega}$ and the $\boldsymbol{v}$ can also be replaced with the dimensionless vorticity vector $\boldsymbol{\omega}^* = \boldsymbol{\omega} \cdot D/U_0$ and the dimensionless velocity vector $\boldsymbol{v}^* = \boldsymbol{v}/U_0$, respectively. Then, Eq. (1), accounting for the acoustic pressure at the microphone location of 90°, can be expressed as[23]

$$p(\boldsymbol{r}, t) \approx \frac{-\rho r_y U_0^2}{4\pi c_\infty D |\boldsymbol{r}|^2} \int_V \frac{\partial}{\partial t}(\boldsymbol{\omega}^* \times \boldsymbol{v}^*)(\boldsymbol{x}, \tau) \cdot \nabla \varphi_y(\boldsymbol{x}) \mathrm{d}V, \qquad (2)$$

where r_y is the distance between the microphone and the cylinder along y-axis, and velocity potential φ_y can be theoretically expressed as[24]

$$\varphi_y = -(D/2)^2 \frac{y}{x^2 + y^2}. \qquad (3)$$

In practice, the influence of force fluctuations in the spanwise direction can be accounted for by a correlation length L_m.[25] Then, Eq. (2) can be written as

$$p(\boldsymbol{r}, t) \approx \frac{-\rho r_y U_0^2 L_m}{4\pi c_\infty D |\boldsymbol{r}|^2} \int_x \int_y \frac{\partial}{\partial t}(\boldsymbol{\omega}^* \times \boldsymbol{v}^*)((x, y), \tau) \cdot \nabla \varphi_y(x, y) \mathrm{d}x\mathrm{d}y. \qquad (4)$$

For simplicity, the integration that can be evaluated by the flow data from the TR-PIV measurement is denoted as G^*,

$$G^*((x, y), \tau) = \frac{\partial}{\partial t}\left((\omega_z^* \cdot v_x^*)((x, y), \tau) \frac{\partial \varphi_y(x, y)}{\partial y} - (\omega_z^* \cdot v_y^*)((x, y), \tau) \frac{\partial \varphi_y(x, y)}{\partial x}\right), \qquad (5)$$

where v_x^* and v_y^* are the dimensionless velocity components in the x direction and y direction, respectively.

III. EXPERIMENT SETUP

A. Anechoic wind tunnel facility and test model

The noise, force, and flow field measurements of the cylinder model were conducted in an anechoic wind tunnel (UNITED) at HKUST.[3] As shown in Fig. 1(a), an open-jet test section was used for the wind tunnel tests. The nozzle of the wind tunnel has a square cross section with a side length of 0.4 m. The turbulence intensity is lower

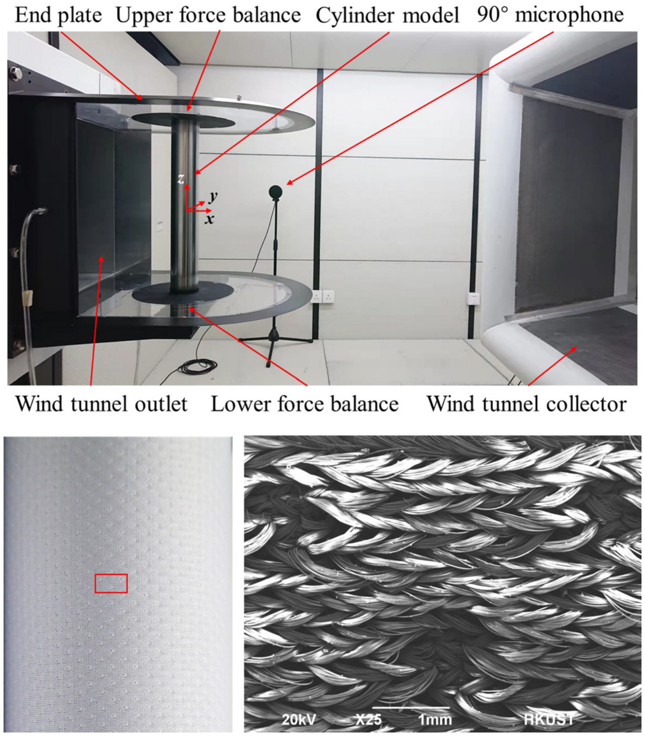

FIG. 1. (a) Experimental setup for the cylinder wind tunnel test. (b) Dimple fabric and its image of scanning electron microscopy.

than 0.25%. The test section is enclosed by a $3.2 \times 3.1 \times 2\ \mathrm{m}^3$ anechoic chamber with a cutoff frequency of 200 Hz.

As shown in Fig. 1(a), a circular cylinder with a diameter of $D = 0.064$ m and a length of $L = 0.4$ m was used as the test model in the anechoic wind tunnel. The model was installed on two end plates, yielding a solid blockage ratio of 16% and an aspect ratio of $L/D = 6.25$. The free-stream velocity U_0 in the wind tunnel tests ranged from 6 to 34 m/s, corresponding to the diameter-based Reynolds numbers ($Re = U_0 D/\nu$ where ν is the kinematic viscosity) between 2.5×10^4 and 1.4×10^5.

The coordinate system follows the convention: the center of the circular cylinder is set as the origin; x represents the streamwise direction; y represents the transverse direction; and z represents the spanwise direction. Figure 1(b) shows the picture of dimple structures knitted on a piece of fabric (left side) and their microscopic photograph (right side). The dimple structure has a diameter of 1 mm with a depth of 0.4 mm. The dimple structures were knitted on the fabric, forming multiple rows along the spanwise direction with a staggered arrangement. The circumferential distance between two adjacent rows is 1.5 mm, and within each row, the spanwise distance between two adjacent dimples is 3 mm.

B. Force, noise, and TR-PIV measurement

For the aerodynamic force measurement, two JR3 20E12A4-125-EF mFS force balances were installed and connected to the circular cylinder model. The sampling frequency for the force measurements was 5 kHz, and the sampling time was 10 s. The force balance was calibrated by adding dead weights, and the results show it has a nominal accuracy of ±0.25% within the measurement range. The repeatability of the force measurement was evaluated to be ± 0.1 N at a confidence level of 95%. Moreover, the aerodynamic force measurement has also been validated by the force measurement on a smooth cylinder,[3] as the force coefficients of about 1.2 are consistent with the previous studies.[24]

For the acoustic measurements, a 1/2-inch G.R.A.S-type 46AE microphone was placed 1.9 m away from the center of the cylinder at an observation angle of 90°. The 24-bit National Instrument PXIe-4497 card was used for the signal acquisition. The microphone was also calibrated by a pistonphone at 94 dB/kHz, and the measurement uncertainty is about ± 0.4 dB at a level of confidence of 95%. For each measurement, the sampling frequency was 50 kHz, and the sampling time was 20 s.

Figure 2 shows the setup for the TR-PIV measurement. The seeding particle is made of Di-Ethyl-Hexyl-Sebacat (DEHS), yielding a mean diameter of 0.3 μm. A double cavity Nd:YLF laser delivers a 527 nm, 20 mJ laser sheet with a thickness of 1.5 mm, located at the mid-span of the cylinder ($z = 0$). The light scattered by the seeding particles was recorded by a SpeedSense M310 CMOS high-speed camera (1280 × 800). The field of view (FOV) has a dimension of $x/D = 2.75$ and $y/D = 1.72$, resulting in a pixel resolution of 138 mm/pixel for the measurement. Under the double-frame mode, the acquisition frequency was 1600 Hz, and each sequence was recorded for a duration of 2.5 s, accounting for 4000 images in each measurement. For the data processing, the size of the adaptive interrogation windows ranged from 16 pixels to 64 pixels with a grid step size of 16 pixels.

Moreover, the microphone measurement and TR-PIV measurement were conducted simultaneously to show the correlations between the far-field noise and the near-flow field. Trigger signals controlled by a timer box were used to synchronize the TR-PIV system and the microphone. After the measurement, the cross-correlation coefficients $R_{G,p}(x, y, t)$ between the sound sources $G^*(x, y, t)$ in the flow field

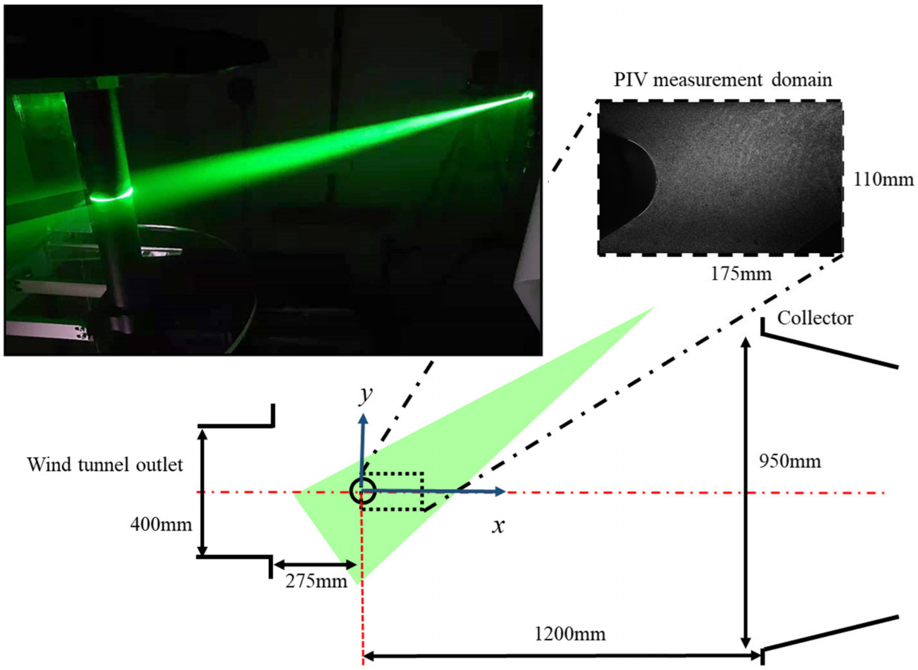

FIG. 2. Experiment setup of the TR-PIV measurement in the UNITED wind tunnel.

and acoustic pressure in the far field are calculated. The $R_{G,p}(x,y,t)$ can be calculated by the expression

$$R_{G,p}(x,y,t) = \frac{\sum_{i=1}^{N}[G^*(x,y,\tau)\cdot p(t)]}{\sigma_G(x,y)\cdot\sigma_p}, \qquad (6)$$

where N is the total number of the measured PIV image pairs, $\sigma_G(x,y)$ is the standard deviation of $G^*(x,y,t)$, and σ_p is the standard deviation of the sound pressure. The time delay τ_d between the TR-PIV measurement and microphone measurement is defined as $\tau_d = t - \tau$.

IV. EFFECTS OF DIMPLES ON DRAG AND NOISE REDUCTIONS

In this study, the drag coefficient C_d is defined as $C_d = 2F_d/\rho U_0^2 DL$, where F_d is the mean drag. The lift fluctuation coefficient C_l' and the drag fluctuation coefficient C_d' are defined as $C_l' = 2F_l'/\rho U_0^2 DL$ and $C_d' = 2F_d'/\rho U_0^2 DL$, respectively, where F_l' is root mean square (RMS) of the lift fluctuation force, and F_d' is RMS of the drag fluctuation force. For the noise measurement results, the overall sound pressure level (*OASPL*) is calculated over a frequency range between 15 Hz and 20 kHz, and the *OASPL* can be normalized by the free-stream velocity: $OASPL^* = OASPL - 10\log_{10}(U_0^6)$ for a fair comparison between different *Re*.[15]

Figure 3 shows the force and noise measurement results for the dimple cylinder. The force measurement results for the smooth cylinder in the Reynolds number ranges from 3.7×10^4 to 1.1×10^5 can be found in the authors' previous work. Compared with the results for the smooth cylinder ($C_d \approx 1.2$), C_d of the dimple cylinder has dramatic drops to a minimum value of about 0.7 at $Re = 8.4 \times 10^4$, after which the C_d slightly increases at higher Reynolds numbers. As the dramatic changes of C_d are associated with the flow transition either in the shear layers or in the boundary layers, the cylinder flow can be classified into different flow regimes at different Reynolds numbers. Following the conventions for defining flow regimes,[26] the sub-critical regime is characterized by the constant C_d; the critical regime is featured by the sudden and continuous drop of C_d to the lowest point; the supercritical regime is defined by the gradual increase in C_d after the minimum point. The classifications of the flow regimes for the dimple cylinder are summarized in Table I, facilitating the following discussions.

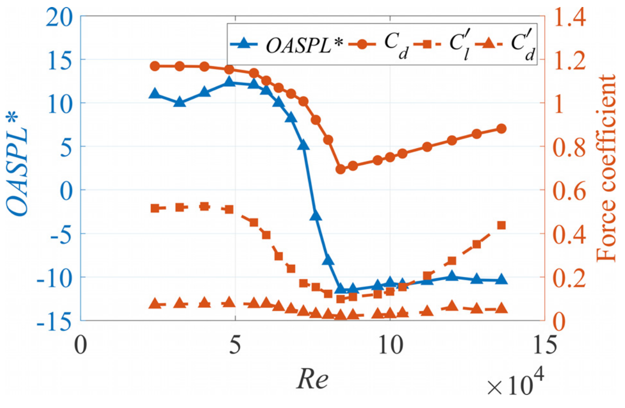

FIG. 3. Force and noise measurement results for the dimple cylinder at different *Re*.

TABLE I. The classifications of the flow regimes for dimple cylinder.

Sub-critical regime	Critical regime	Supercritical regime
$Re < 6.0 \times 10^4$	$6.0 \times 10^4 < Re < 8.8 \times 10^4$	$Re > 8.8 \times 10^4$

The variations of noise and drag follow similar trends in each flow regime, showing that the dimple fabric attached to the cylinder reduces drag and noise simultaneously. In the sub-critical regime, the values for C_d, $OASPL^*$, and C_l' remain almost unchanged. Compared to the results for the smooth cylinder in the similar Reynolds number range,[3] the critical regime for the dimple cylinder features dramatic drops in C_d, $OASPL^*$, and C_l'. In particular, all the variables reach their lowest value at the end of the critical regime ($Re = 8.4 \times 10^4$). In the supercritical regime, C_l' shows a upward trend, which is responsible for the increased $OASPL^*$, as the C_l' is the main influential parameter that impacts the cylinder noise.[27]

The sound pressure level (*SPL*) of the dimple cylinder is also compared in different flow regimes to explore the direct reasons for the changes in $OASPL^*$. As shown in Fig. 4, the clear peak located at $St = 0.19$ represents the strong Aeolian tone, which is similar to the

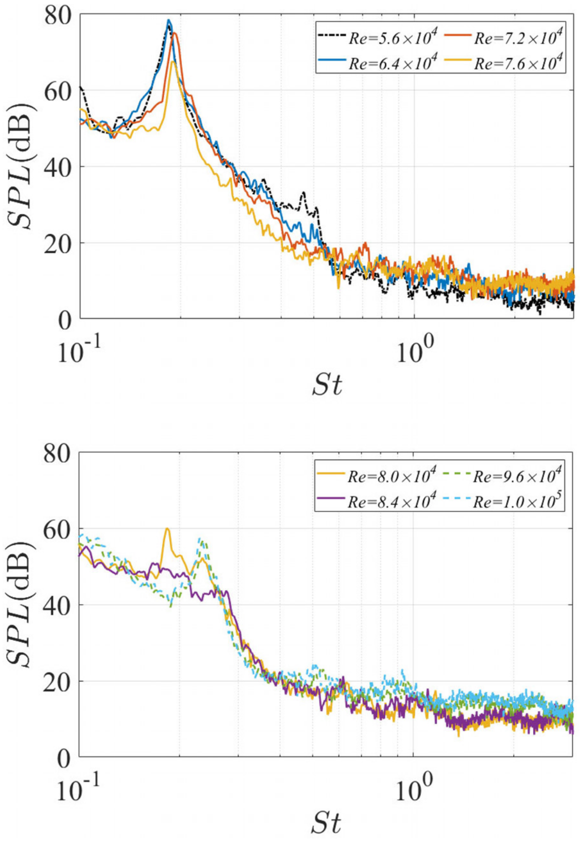

FIG. 4. The sound pressure level of the dimple cylinder in (a) sub-critical and critical flow regimes and (b) critical and supercritical flow regimes. Here, the solid lines donate the cylinder flow in the critical regime.

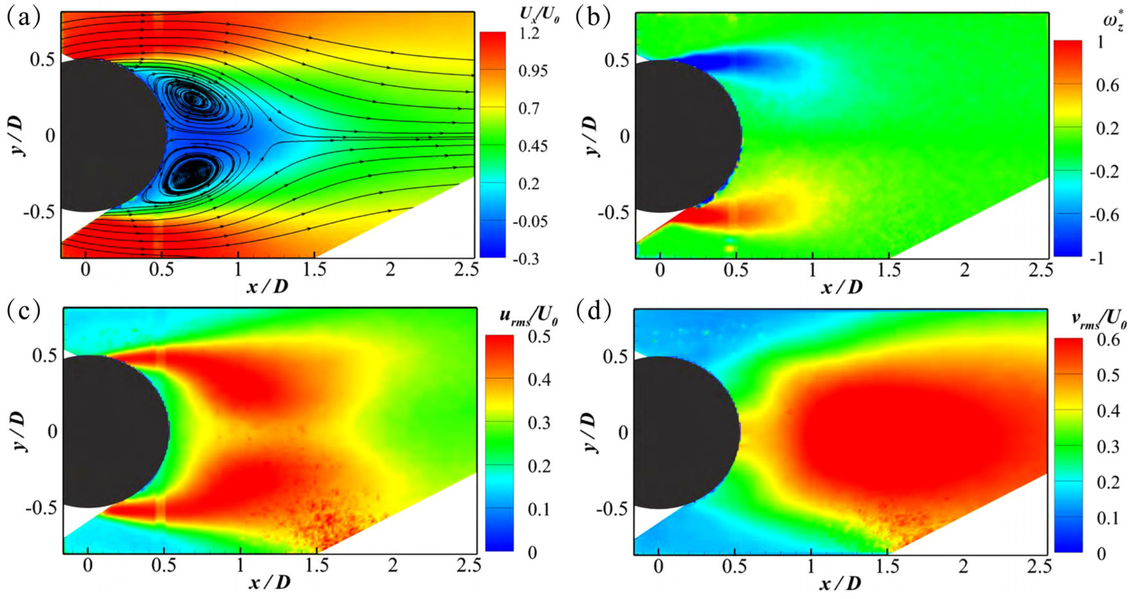

FIG. 5. The TR-PIV measurement results for the smooth cylinder at $Re = 9.6 \times 10^4$: (a) U_x/U_0 distributions with time-average streamlines; (b) time-average vorticity ω_z^*; (c) streamwise velocity fluctuations u_{rms}/U_0; and (d) vertical velocity fluctuations v_{rms}/U_0.

Aeolian tone of the smooth cylinder in the sub-critical regime.[3] In the critical regime, the gradual suppression of the Aeolian tone is the main reason for the noise reductions. In particular, no clear peak can be found at $Re = 8.4 \times 10^4$, corresponding to the lowest $OASPL^*$. By contrast, the Aeolian tone reappears at a higher Strouhal number ($St \approx 0.23$) but with low amplitudes. For this reason, the $OASPL^*$ has slight increases in this flow regime.

V. TR-PIV MEASUREMENT

A. Flow structures

Figure 5(a) shows the time-average streamwise velocity U_x/U_0 and the time-average streamlines for the smooth cylinder at $Re = 9.6 \times 10^4$. The low-speed flow region featured by the mean flow recirculation (streamlines) is formed behind the cylinder, by which the low-pressure region is formed on the rear of the cylinder, and thus the production of pressure drag. As shown in Fig. 5(b), the dimensionless spanwise vorticity $\omega_z^* = \omega_z D/U_0$ (ω_z is the time-average vorticity along the z axis) presents the existence of the shear layers which produce vortex motions during the vortex shedding process. Figure 5(c) shows the distributions of the streamwise velocity fluctuations u_{rms}/U_0, which manifest a dual peak pattern, and the high u_{rms}/U_0 is mainly caused by the strong shear layer mixing during the vortex shedding process. Moreover, as shown in Fig. 5(d), the strong vertical velocity fluctuations v_{rms}/U_0 near the cylinder's central plane represent the strong flow entrainment during the vortex shedding process.

By comparison, Fig. 6 shows the distributions of U_x/U_0 and the time-average streamlines for the dimple cylinder in different flow regimes. In the critical regime, the wakes become narrower, and the separation points on the cylinder are delayed downstream, which explains the drops in C_D. At $Re = 8.4 \times 10^4$, one distinct flow feature is the asymmetric wake. As the flow transitions are highly sensitive to experimental conditions, e.g., surface roughness, this asymmetric flow is likely to be caused by the separation bubble appearing first on one side of the cylinder.[28] In addition, the recirculation regions, whose length is quantified by the saddle points (red marks in Fig. 6), are elongated significantly in the critical and supercritical regime, suggesting the interactions or flow entrainment between two shear layers become weak compared to that in the sub-critical regime.

Figure 7 presents the ω_z^* distributions for the dimple cylinder in different flow regimes. In the sub-critical regime [Fig. 7(a)], the ω_z^* is symmetrically distributed, which is similar to that of the smooth cylinder in the sub-critical regime [see Fig. 5(b)]. In the critical regime [Figs. 7(b)–7(d)], the shear layers are extended before rolling up, and the values of ω_z^* become lower compared to that of the smooth cylinder. These results suggest that the shear layers tend to be stabilized in the critical regime, causing the increased recirculation length in Fig. 6. In particular, at $Re = 8.4 \times 10^4$ [Fig. 7(d)], the distributions of ω_z^* become asymmetric when the separation bubble appears. It breaks the dynamic similarity between two shear layers,[29] which is the reason for the weak shear-layer interactions. By contrast, in the supercritical regime, the wakes recover symmetric again, suggesting that the dynamic similarity between two shear layers is reestablished. Compared to the smooth cylinder, the shear layers are elongated downstream, but the distance between them becomes less, which explains the narrowed wake deficits in this flow regime.

To represent the vortex shedding strength, Fig. 8 shows the distributions of v_{rms}/U_0 for the dimple cylinder. In the sub-critical regime, the values of v_{rms}/U_0 become high around the cylinder's central plane. The strong vertical flow is mainly induced by the alternative roll-up of the shear layers during the formation of the Kármán vortex.

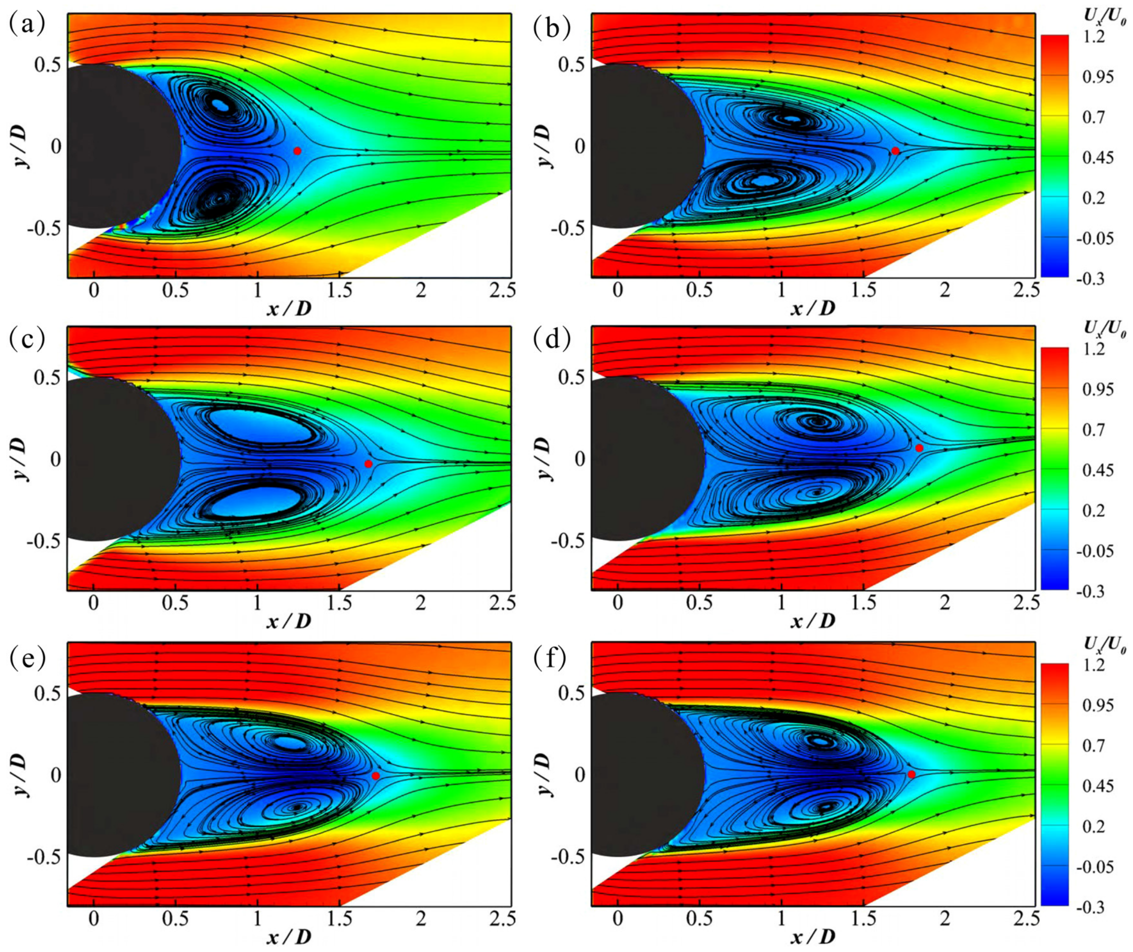

FIG. 6. Non-dimensional time-average streamwise velocity U_x/U_0 and its streamlines for the dimple cylinder at (a) $Re = 5.6 \times 10^4$ (sub-critical); (b) $Re = 7.2 \times 10^4$ (critical); (c) $Re = 7.6 \times 10^4$ (critical); (d) $Re = 8.4 \times 10^4$ (critical); (e) $Re = 9.6 \times 10^4$ (supercritical); and (f) $Re = 1.0 \times 10^5$ (supercritical).

By contrast, v_{rms}/U_0 is significantly reduced in the critical regime [Figs. 8(b)–8(d)], corresponding to the weak strength of vortex shedding. In the supercritical regime [Fig. 8(e) and 8(f)], the v_{rms}/U_0 near the saddle points has slight increases compared to those in the critical regime, which suggests the regeneration of the regular vortex shedding when the dynamic similarity between two shear layers is reestablished. This result also explains the reappearance of the Aeolian tone in the noise spectra [Fig. 4(b)]. However, values of v_{rms}/U_0 are still low, identical to the low amplitudes of the Aeolian tone in the supercritical regime, as the regenerated vortex shedding has a low strength.

B. Sound sources in flow fields

The previous discussions on the TR-PIV measurement results show that the noise reductions on the dimple cylinder are related to the significant changes in wake structures. This section aims to investigate the sound sources in flow fields, which can be used to explain noise reductions directly.

The root mean square of G^*_τ (G^*_{rms}) is calculated to represent the statistical mean of sound sources. Figure 9 shows the distributions of G^*_{rms} for the smooth cylinder at $Re = 9.6 \times 10^4$, and the dashed rectangles enclose the sound source close to the separation points (circumferential angle of 90°–130° from the forward stagnation point.[30]) The predominant finding is that sound sources are mainly concentrated around the separation points close to the cylinder surface (within the dashed rectangle). This result is reasonable as the strong sound sources are associated with the unsteady vortex motions near the cylinder surface. During the vortex shedding process, the unsteady vortex motions are mainly induced by the entrainment and oscillation of the shear layers,[23,31] which is closely associated with the occurrence of fluctuating force as shown in Fig. 3. By contrast, the sound sources are significantly reduced in the wake away from the cylinder surface. Since ϕ_y represents the effect of noise scattering at the cylinder surface, it is natural that the unsteady vortex motion near the cylinder surface is more important in noise generations.[23]

The time-varying signals of G^*_τ were recorded at two measurement locations, which are symmetrically placed at $x/D = 0.20$ and

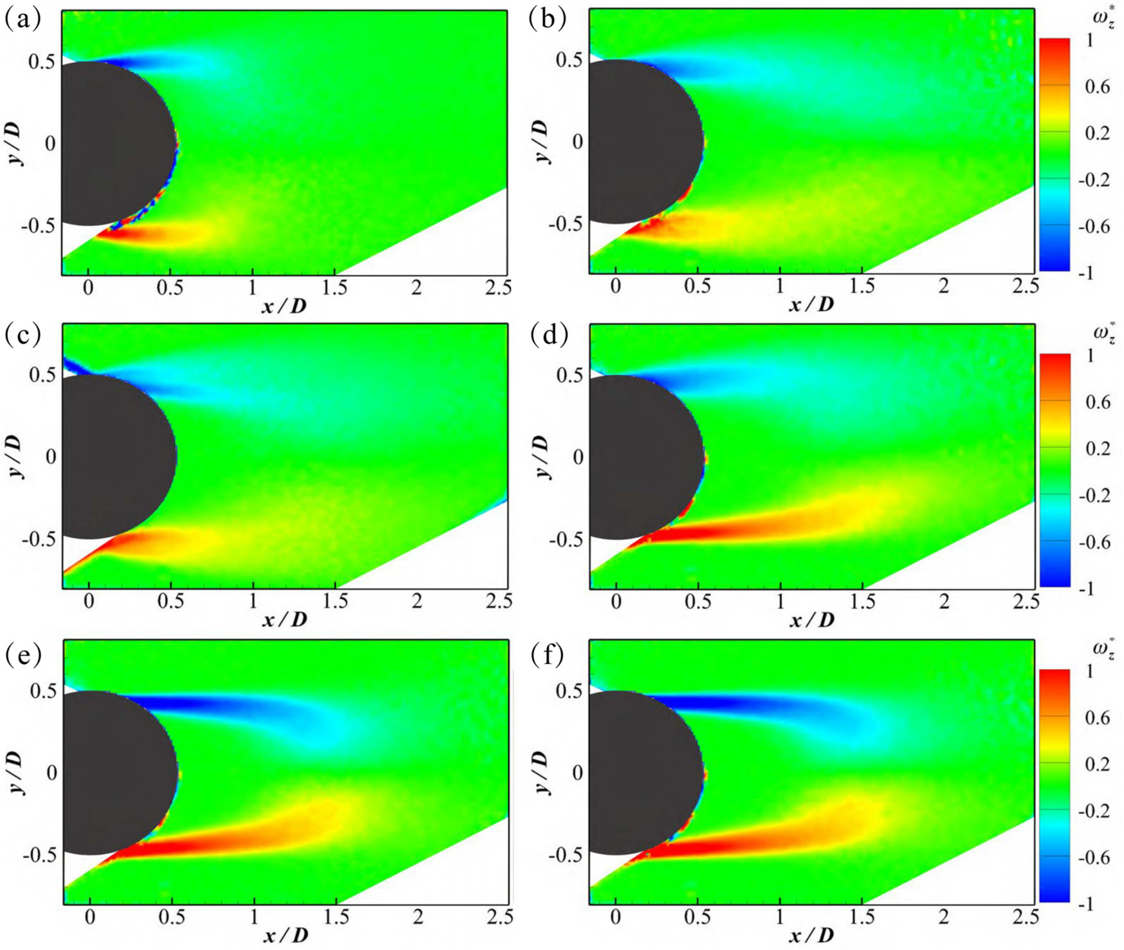

FIG. 7. Non-dimensional time-average spanwise vorticity ω_z^* for the dimple cylinder at (a) $Re = 5.6 \times 10^4$ (sub-critical); (b) $Re = 7.2 \times 10^4$ (critical); (c) $Re = 7.6 \times 10^4$ (critical); (d) $Re = 8.4 \times 10^4$ (critical); (e) $Re = 9.6 \times 10^4$ (supercritical); and (f) $Re = 1.0 \times 10^5$ (supercritical).

$y/D = -0.54$ and 0.54, respectively. Figure 10(a) shows the spectral density of G_τ^*, where the peaks are located at $St \approx 0.19$, coinciding with the St of the Aeolian tone. Figure 10(b) shows the raw signals of G_τ^*, which was filtered with a passband from $St = 0.1$ to $St = 0.3$ to isolate signals related to the Aeolian tone. The raw signals show periodic features corresponding to the alternative form of Kármán vortex. Moreover, since the correlation coefficient between these two signals was calculated to be -0.8, they have near amplitude, but with opposite phases. Therefore, the changes in the sound sources on one side produce a monopole source. With two monopole sources of equal strength but opposite phases, the cylinder noise represents the typical feature of a dipole source.

Based on Eq. (6), we further reveal the direct correlations between the far-field noise and the near-field sound sources by calculating the $R_{G,p}(x, y, t)$ between the G_τ^* from TR-PIV and p from the microphone measurements. Before the calculations, τ_d is first evaluated, considering the sound propagation and the delay of the equipment. As shown in Fig. 11(a), the temporal evolution of $R_{G,p}(\tau_d)$ at $x/D = 0.20$ and $y/D = 0.54$ is calculated by the cross-correlation at different time delay τ_d. The red asterisk represents the recognized local maximum, which exhibits a periodic feature due to the vortex shedding. The maximum $R_{G,p}(\tau_d)$ is recognized at $\tau_d = 25.6$ ms, which can be considered as the real-time delay between the TR-PIV and microphone measurement. Consequently, the spatial distributions of $R_{G,p}(x, y, t)$ are calculated at this time delay.

As shown in Fig. 11(b), high $R_{G,p}(x, y)$ are found within the shear layers near the cylinder's surface. Both opposite signs of the $R_{G,p}(x, y)$ existed on each side of the cylinder, representing the opposite phases of the sound sources. In addition, the high amplitude in the cylinder's wake represents downstream developments of the sound sources originating from the last shedding period. Even if results show high correlations in this area, as it is away from the cylinder's surface, its contribution to sound generation is negligible. In general, the cross-correlation results provide direct evidence of the strong sound sources that exist in the flow fields near the cylinder surface.

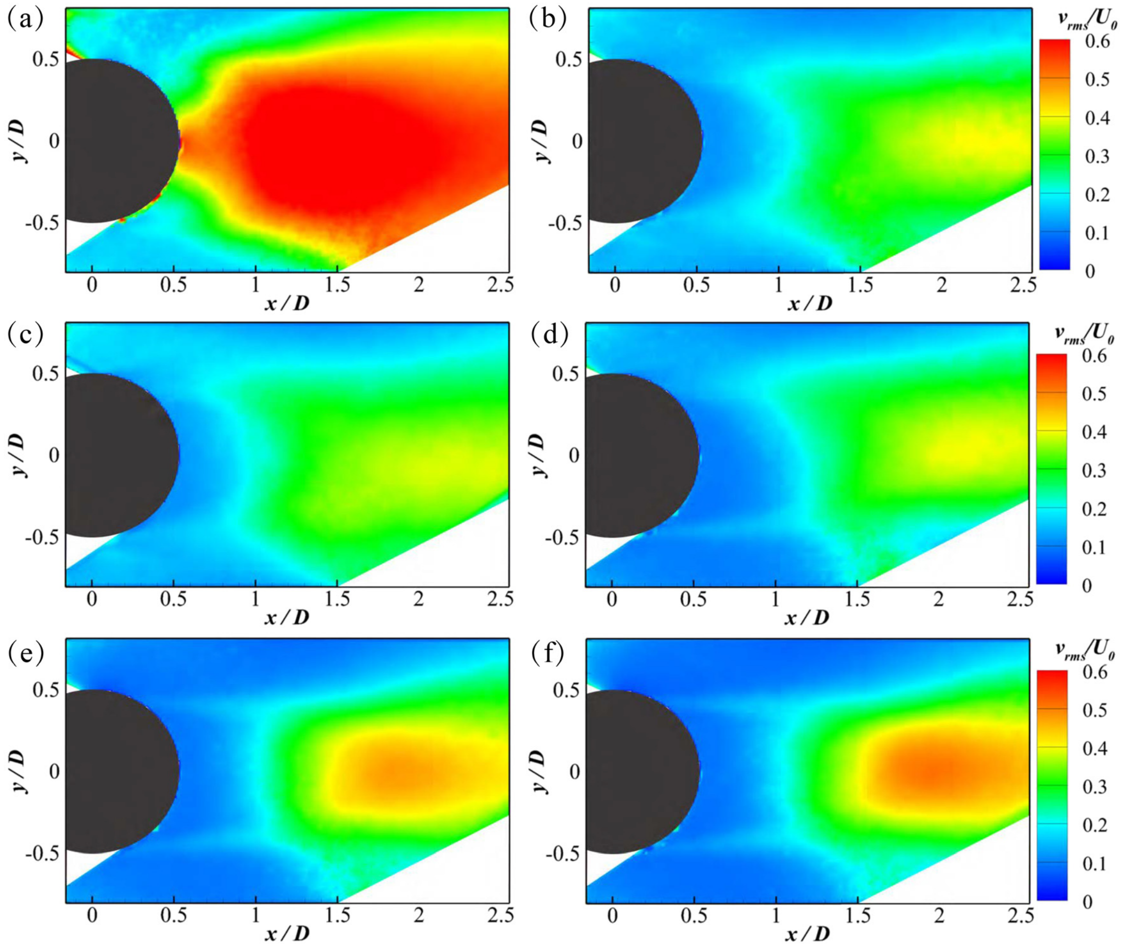

FIG. 8. Vertical velocity fluctuation density v_{rms}/U_0 for the dimple cylinder at (a) $Re = 5.6 \times 10^4$ (sub-critical); (b) $Re = 7.2 \times 10^4$ (critical); (c) $Re = 7.6 \times 10^4$ (critical); (d) $Re = 8.4 \times 10^4$ (critical); (e) $Re = 9.6 \times 10^4$ (supercritical); and (f) $Re = 1.0 \times 10^5$ (supercritical).

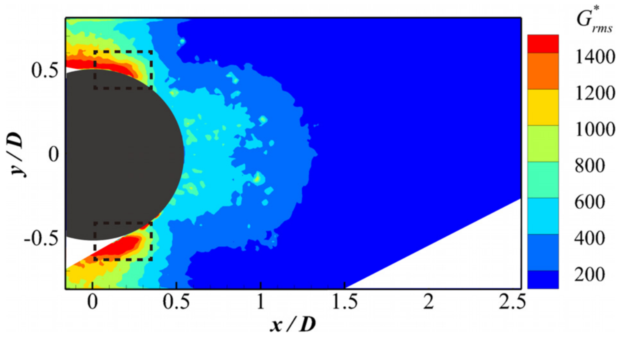

FIG. 9. Distributions of G^*_{rms} for the smooth cylinder at $Re = 9.6 \times 10^4$.

Figure 12 shows the distributions of G^*_{rms} for the dimple cylinder flow, and the dashed rectangles enclose the sound sources near the separation locations. In the sub-critical regime [Fig. 12(a)], the strong sound sources are concentrated within the dashed rectangle near the separation locations, similar to those for the smooth cylinder in the sub-critical regime. With the noise reductions in the critical regime, the sound sources near the separation locations are significantly reduced [see Figs. 12(b)–12(d)]. The reductions in sound sources suggest that the unsteady vortex motions, especially near the cylinder surface, tend to be stabilized, which is closely associated with the suppression of vortex shedding (Fig. 8). The stabilized vortex motions near the cylinder surface also cause reduced pressure fluctuations, which are manifested by the drops of lift fluctuation coefficients in Fig. 3. For this reason, the Aeolian tone is suppressed and thus, cylinder noise is significantly reduced in the critical regime of the dimple cylinder.

As shown in Figs. 9(e) and 9(f), although the cylinder noise has slight increases in the supercritical regime (see Fig. 3), the amplitudes of sound sources near the cylinder surface are even lower in the supercritical regime. It is noted that previous studies[15,27] show that the vortex shedding in the supercritical regime demonstrates three-dimensional features, which cause the spanwise segments of pressure fluctuations along the cylinder surface. As a result, the sound source

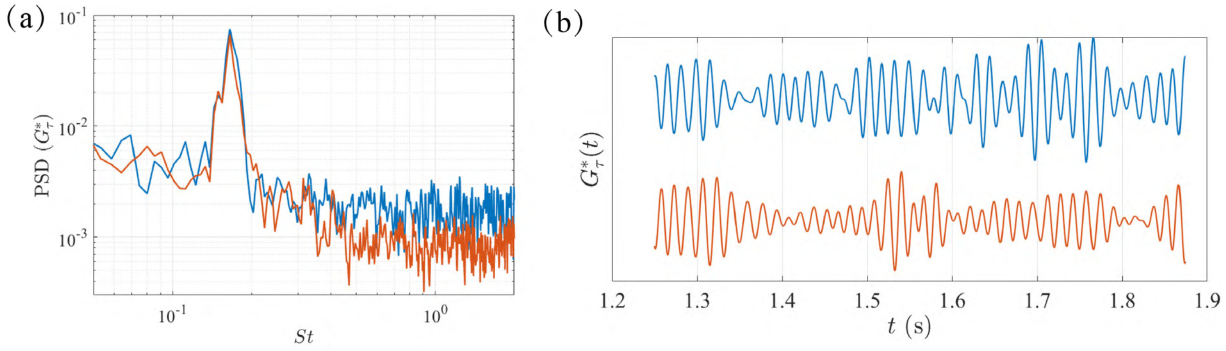

FIG. 10. (a) Power spectral density of G_τ^* at two measurement locations. (b) Time-varying signals of G_τ^* at two measurement locations. Here, blue color represents the results at $x/D = 0.20$ and $y/D = 0.54$, and orange color represents the result at $x/D = 0.20$ and $y/D = 0.54$.

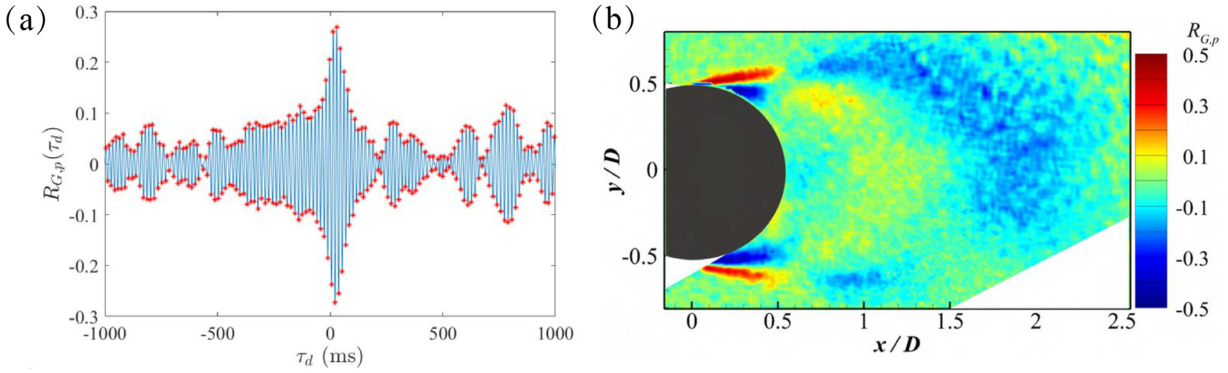

FIG. 11. (a) Temporal evolution of the cross-correlation coefficient $R_{G,p}(\tau_d)$ at $x/D = 0.20$ and $y/D = 0.54$. (b) Distributions of $R_{G,p}$ for the smooth cylinder at $Re = 1.0 \times 10^5$.

along the spanwise direction of the cylinder is out of phase, which also influences the far-field noise because of the effects of the destructive interference.[32] Simply analyzing the noise sources in a single plane may not fully explain the complex flow dynamics and noise mechanism in the supercritical regime. Therefore, fully establishing the quantitative relation [Eq. (4)] between the sound sources in flow fields and the far-field noise in the critical and supercritical regimes requires information on the instantaneous flow fields over the whole span of the dimple cylinder, which is still a challenging problem. Nevertheless, the flow field measurements and analysis in this study reveal that noise reductions on the dimple cylinder are directly explained by the decreased sound sources (unsteady vortex motions) near the cylinder surface, which is also associated with changes in vortex shedding strength in the wake.

VI. CONCLUSIONS

This study investigates the effects of dimples on drag and noise reductions of a circular cylinder. The force and noise measurement results show that dimples built on a piece of fabric attached to the cylinder can simultaneously reduce drag and noise. First, the wake structures of the dimple cylinder in different flow regimes were investigated by the TR-PIV measurements. The wake becomes narrower in the critical flow regime, corresponding to the continuous drops in C_d. The v_{rms}/U_0 in the near-wake region is significantly reduced in the critical flow regime, suggesting the suppression of the vortex shedding. In the supercritical regime, the wake was recovered to symmetry with slight increases in v_{rms}/U_0 in the near-wake region, suggesting the reappearance of vortex shedding. Second, based on the vortex sound theory, the flow analysis shows that the dominant sound sources are concentrated near the cylinder surface. The strong sound sources are caused by the unsteady vortex motions near the separation locations during the process of vortex shedding. In particular, the increases in the sound source on one side are synchronized with its decreases on the other side, resulting in a dipole sound source of the cylinder. The cross-correlations between the near-field flow measurements (TR-PIV) and the far-field noise (microphone measurement) provide direct evidence that the cylinder noise is associated with strong sound sources near the cylinder surface. Finally, flow analysis on the dimple cylinder flow reveals that the decreases in sound sources near the cylinder surface can directly explain the noise reductions in the critical and supercritical regimes, which is also associated with the reduced strength of the vortex shedding.

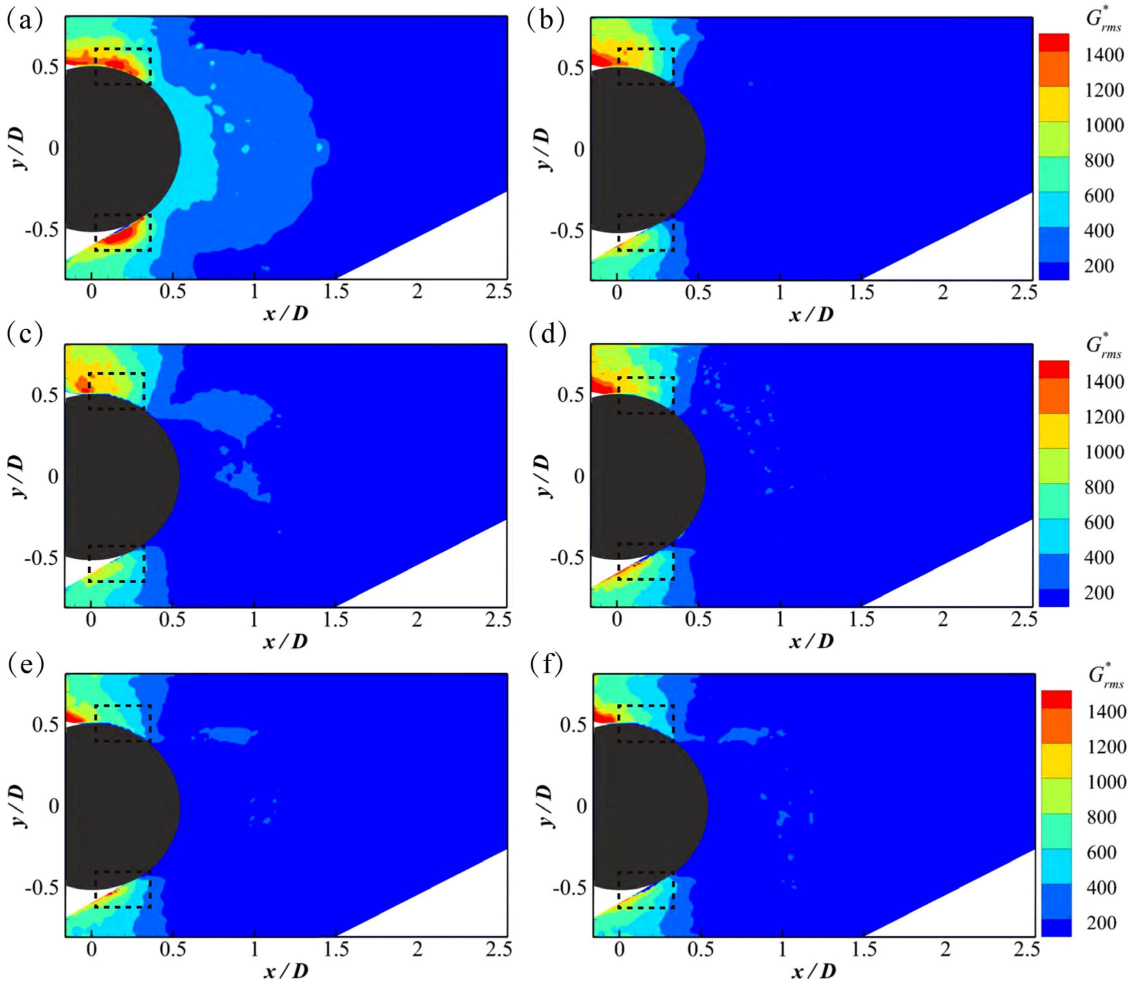

FIG. 12. Distributions of G^*_{rms} for the dimple cylinder at: (a) $Re = 5.6 \times 10^4$ (sub-critical); (b) $Re = 7.2 \times 10^4$ (critical); (c) $Re = 7.6 \times 10^4$ (critical); (d) $Re = 8.4 \times 10^4$ (critical); (e) $Re = 9.6 \times 10^4$ (supercritical); and (f) $Re = 1.0 \times 10^5$ (supercritical).

ACKNOWLEDGMENTS

This work was partially supported by the Hong Kong Innovation and Technology Commission (No. ITS/354/18FP) and the A. Kwok Sports Aerodynamics Science Initiative. The authors would also like to thank the Hong Kong Sports Institute for the support of this work. The study was conducted in the Aerodynamics Acoustics & Noise Control Technology Centre (AANTC) at the Hong Kong University of Science and Technology (http://aantc.ust.hk).

AUTHOR DECLARATIONS

Conflict of Interest

The authors have no conflicts to disclose.

Author Contributions

Chuntai Zheng: Conceptualization (equal); Formal analysis (equal); Investigation (equal); Methodology (equal); Writing – original draft (equal). **Peng Zhou:** Investigation (equal); Writing – review & editing (equal). **Siyang Zhong:** Supervision (equal); Writing – review & editing (equal). **Xin Zhang:** Project administration (lead); Resources (lead); Supervision (lead); Writing – review & editing (lead).

DATA AVAILABILITY

The data that support the findings of this study are available from the corresponding author upon reasonable request.

REFERENCES

[1] H. Choi, W.-P. Jeon, and J. Kim, "Control of flow over a bluff body," Annu. Rev. Fluid Mech. **40**, 113–139 (2008).

[2] E. Achenbach and E. Heinecke, "On vortex shedding from smooth and rough cylinders in the range of Reynolds numbers 6×10^3 to 5×10^6," J. Fluid Mech. **109**, 239–251 (1981).

[3] C. Zheng, P. Zhou, S. Zhong, X. Zhang, X. Huang, and R. C.-H. So, "An experimental investigation of drag and noise reduction from a circular cylinder using longitudinal grooves," Phys. Fluids **33**(11), 115110 (2021).

[4] Y. Z. Liu, L. L. Shi, and J. Yu, "TR-PIV measurement of the wake behind a grooved cylinder at low Reynolds number," J. Fluids Struct. **27**(3), 394–407 (2011).

[5] Y. Yamagishi and M. Oki, "Effect of groove shape on flow characteristics around a circular cylinder with grooves," J. Visualization **7**(3), 209–216 (2004).

[6] N. Fujisawa, K. Hirabayashi, and T. Yamagata, "Aerodynamic noise reduction of circular cylinder by longitudinal grooves," J. Wind Eng. Ind. Aerodyn. **199**, 104129 (2020).

[7] P. Bearman and J. Harvey, "Control of circular cylinder flow by the use of dimples," AIAA J. **31**(10), 1753–1756 (1993).

[8] S. Huang, "VIV suppression of a two-degree-of-freedom circular cylinder and drag reduction of a fixed circular cylinder by the use of helical grooves," J. Fluids Struct. **27**(7), 1124–1133 (2011).

[9] T. F. Geyer and E. Sarradj, "Circular cylinders with soft porous cover for flow noise reduction," Exp. Fluids **57**(3), 1–16 (2016).

[10] S. A. Showkat Ali, X. Liu, and M. Azarpeyvand, "Bluff body flow and noise control using porous media," AIAA Paper No. AIAA 2016-2754, 2016.

[11] C. Apelt, G. West, and A. A. Szewczyk, "The effects of wake splitter plates on the flow past a circular cylinder in the range $10^4 < R < 5 \times 10^4$," J. Fluid Mech. **61**(1), 187–198 (1973).

[12] R. Octavianty and M. Asai, "Effects of short splitter plates on vortex shedding and sound generation in flow past two side-by-side square cylinders," Exp. Fluids **57**(9), 1–13 (2016).

[13] B. Chen, X. Yang, G. Chen, X. Tang, J. Ding, and P. Weng, "Numerical study on the flow and noise control mechanism of wavy cylinder," Phys. Fluids **34**(3), 036108 (2022).

[14] Y. Xing, P. Liu, H. Guo, and L. Li, "Effect of helical cables on cylinder noise control," Appl. Acoust. **122**, 152–155 (2017).

[15] R. Blevins, "Review of sound induced by vortex shedding from cylinders," J. Sound Vib. **92**(4), 455–470 (1984).

[16] Y. Zhang, J. Zhang, T. Li, and L. Zhang, "Investigation of the aeroacoustic behavior and aerodynamic noise of a high-speed train pantograph," Sci. China Technol. Sci. **60**(4), 561–575 (2017).

[17] T. Sueki, T. Takaishi, M. Ikeda, and N. Arai, "Application of porous material to reduce aerodynamic sound from bluff bodies," Fluid Dyn. Res. **42**(1), 015004 (2010).

[18] A. Powell, "Theory of vortex sound," J. Acoust. Soc. Am. **36**(1), 177–195 (1964).

[19] M. Howe, "The generation of sound by aerodynamic sources in an inhomogeneous steady flow," J. Fluid Mech. **67**(3), 597–610 (1975).

[20] F. Duan and J. Wang, "Fluid–structure–sound interaction in noise reduction of a circular cylinder with flexible splitter plate," J. Fluid Mech. **920**, A6 (2021).

[21] T. Uda, A. Nishikawa, S. Someya, and A. Iida, "Prediction of aeroacoustic sound using the flow field obtained by time-resolved particle image velocimetry," Meas. Sci. Technol. **22**(7), 075402 (2011).

[22] M. S. Howe and M. S. Howe, *Theory of Vortex Sound* (Cambridge University Press, 2003).

[23] T. Takaishi, M. Ikeda, and C. Kato, "Method of evaluating dipole sound source in a finite computational domain," J. Acoust. Soc. Am. **116**(3), 1427–1435 (2004).

[24] M. M. Zdravkovich, *Flow Around Circular Cylinders: Volume 2: Applications* (Oxford University Press, 1997), Vol. 2.

[25] O. Phillips, "The intensity of Aeolian tones," J. Fluid Mech. **1**(6), 607–624 (1956).

[26] E. Achenbach, "Influence of surface roughness on the cross-flow around a circular cylinder," J. Fluid Mech. **46**(2), 321–335 (1971).

[27] H. Fujita, "The characteristics of the Aeloian tone radiated from two-dimensional cylinders," Fluid Dyn. Res. **42**(1), 015002 (2010).

[28] H. Higuchi, H.-J. Kim, and C. Farell, "On flow separation and reattachment around a circular cylinder at critical Reynolds numbers," J. Fluid Mech. **200**, 149–171 (1989).

[29] S. Singh and S. Mittal, "Flow past a cylinder: Shear layer instability and drag crisis," Int. J. Numer. Methods Fluids **47**(1), 75–98 (2005).

[30] E. Achenbach, "Distribution of local pressure and skin friction around a circular cylinder in cross-flow up to $Re = 5\times 10^6$," J. Fluid Mech. **34**(4), 625–639 (1968).

[31] J. Gerrard, "The mechanics of the formation region of vortices behind bluff bodies," J. Fluid Mech. **25**(2), 401–413 (1966).

[32] J. S. Cox, K. S. Brentner, and C. L. Rumsey, "Computation of vortex shedding and radiated sound for a circular cylinder: Subcritical to transcritical Reynolds numbers," Theor. Comput. Fluid Dyn. **12**(4), 233–253 (1998).